CALPHAD: Computer Coupling of Phase Diagrams and Thermochemistry 95 (2026) 102999

Contents lists available at ScienceDirect

Calphad

journal homepage: www.elsevier.com/locate/calphad

Existence domains for various invariant reactions in FCC binary phase diagrams involving two phases: A quasi-chemical — regular solution approach

Rajendra Prasad Gorrey [a],*, Monish Kumar Dharanilogan [a], Abhishek Kumar Thakur [b]

[a] Department of Metallurgical and Materials Engineering, NIT Andhra Pradesh, Tadepalligudem, West Godavari, Andhra Pradesh, 534101, India
[b] Department of Material Science and Engineering, The University of Arizona, Tucson, AZ 85721, USA

ARTICLE INFO

Keywords:
Existence domain diagrams
Binary solid solutions
Quasi-chemical method
Neural network
Phase diagram

ABSTRACT

For the chosen thermodynamic model, the topology of the phase diagram depends on the thermodynamic parameters of the elements and the selected interaction energy parameters. A systematic variation of the energy parameters can reveal the nature of the phase diagrams obtained under the given conditions. In the present study, the quasi-chemical solution model, which accounts for short range order parameter up to the pair cluster, is adopted for the solid phase, while the regular solution model is used for the liquid phase. Using these solution models, the boundaries of the interaction energy parameters that result in various invariant reactions are calculated for the model system. The regions bounded by these boundaries are referred to as domains. This methodology is applied to the Cu-Ir system. The invariant reaction data obtained from these domains are used to train an artificial neural network model to predict the interaction energy parameters. The phase diagram obtained from the predicted values shows a good agreement with the experimental data. Thus, this methodology provides intelligent initial interaction parameters for the optimization process using experimental data.

1. Introduction

The nature of the phase diagrams obtained for the chosen solution models is strongly dependent on the selected interaction energy parameter set. Van Laar considered different energy parameters w^{α} and w^{β} for the α and β phases, respectively, such that $w^{\alpha} > 0$ and $w^{\beta} > 0$, and calculated binary phase diagrams using the regular solution model [1,2]. The calculated phase diagrams showed various invariant reactions along with a miscibility gap in the α and β phases, depending on the energy parameters. Pelton A T and Thompson W T considered the same regular solution model but extended the domain to negative values of w^{α} and w^{β} as well [3]. They calculated phase diagrams for different values of the interaction energy parameters and showed that invariant reactions such as peritectic, syntectic, and retrograde systems also can be obtained using the regular solution model, as stated by Van Laar. A similar study is also reported by Oonk [4], Dehoff [5] and Chang and Chen [6].

Sarma et al. considered the same regular solution model for the α and β phases and carried out a systematic study to determine the boundaries for various invariant reactions, such as congruent minimum/maximum, eutectic, peritectic, syntectic, and monotectic reactions, by treating the β phase as a liquid phase [7]. The intersection of these invariant reaction boundary lines results in various regions. Based on the permissible region for these invariant reactions and the intersection of the boundary lines, various invariant reactions occur within these regions. These regions are referred to as domains. They considered different thermodynamic parameters, which represent different systems, and showed the variations in these domains. A similar study is also carried out by Thakur et al. for the Nb-Ti system using the cluster variation method [8].

For the solution models such as the cluster variation method [9], cluster site approximation method [10] and FYL–CVM [11–13], which account for short-range order parameters up to the cluster chosen in modelling the phases, the Gibbs or Helmholtz energy of the system is a function of internal variables that help to describe the atomic configuration on the chosen cluster. The energy of the phase must be minimized with respect to these internal variables for the chosen energy parameter set and thermodynamic state to obtain the equilibrium state of the system. This requires solving a system of nonlinear equations. Thus, thermodynamic calculations associated with these models are computationally intensive, unlike those using Redlich–Kister (R-K) polynomials. Sanchez and Mohri proposed a variable-basis cluster

* Corresponding author.
E-mail address: rajendraprasad.mme@nitandhra.ac.in (R.P. Gorrey).

https://doi.org/10.1016/j.calphad.2026.102999
Received 21 April 2026; Received in revised form 2 September 2026; Accepted 3 September 2026
0364-5916/© 2026 Elsevier Ltd. All rights are reserved, including those for text and data mining, AI training, and similar technologies.

expansion to reduce the computational burden associated with this minimization process [14], while Gorrey et al. [15] approximated these internal variables as polynomials similar to the R-K polynomials. Optimization of interaction energy parameters, specific to the phase, using phase equilibrium data, thermodynamic data, or values obtained from theoretical calculations is similar to a least-squares fit. In this case, the error between the observed or experimental value and the calculated value using the thermodynamic model is considered. The correction in the interaction energy parameter of one phase is coupled with the interaction energy parameters of the phases that are in equilibrium with it. This process is highly sensitive to the initial values chosen. The complexity of this process increases with the number of phases considered as well as with the number of energy parameters included in the thermodynamic model [16,17]. Thus, choosing a good set of initial values for these interaction energy parameters is essential for this optimization process. The calculated domain diagrams for different invariant reactions provide the permissible energy values. Thus, based on the invariant reaction in the phase diagram an educated guess of the initial values for the interaction energies can be obtained from these existence domain diagrams.

In the present study, these domains are obtained using the quasi-chemical [18] and regular solution model approximations. The low temperature phase, generally a solid solution, is modelled using the quasi-chemical approximation, which provides short-range order information up to the pair cluster. The high temperature phase, generally the liquid phase, is modelled using the regular solution model. Section 2 deals with the thermodynamics of the low and high temperature phases using the quasi-chemical solution model for the fcc system and the regular solution model, respectively. Calculation of existence domains for various invariant reactions for a model system is also presented. Section 3 presents the analysis of the domains obtained for the prototype system and the behaviour of the system in selected domains. Section 4 presents the application of this method to the Cu-Ir system. For this system, domains of various invariant reactions are obtained. Since the Cu-Ir system exhibits a peritectic reaction, the invariant reaction data is generated from the corresponding domain for different interaction energy parameters. This data is used to train a supervised artificial neural network. The trained neural network is used to predict the interaction energy parameters of the experimental Cu-Ir system, and a comparison of the phase diagrams computed using the predicted values with the experimental phase diagram is presented. Summary and conclusions are presented in Section 5.

2. Existence domain diagrams

2.1. Thermodynamics of the α and β phases

The Gibbs energy expression for a selected phase can be expressed as

$$G^{\alpha} = G^{ref,\alpha} + G^{mix,\alpha}$$

The first term in the above expression refers to the reference energy state. For a binary system consisting of components A and B, it can be written as

$$G^{ref,\alpha} = x_A^{\alpha} G_A^{0,\alpha} + x_B^{\alpha} G_B^{0,\alpha} \tag{1}$$

where $G_i^{0,\alpha}$ represents the standard Gibbs energy of the component i in α phase.
The second term refers to the mixing contributions and can be expressed as

$$G^{mix} = H^{mix} - TS^{mix}$$

The enthalpy of mixing, H^{mix}, is expressed in terms of the pair correlation function, u_2, for the fcc system in the orthogonal basis using quasi-chemical solution approach as

$$H^{mix} = 6w^{\alpha}(u_2 - 1)$$

In the above expression, w^{α} represents the effective pair interaction energy. On rearranging the terms, the expression for the entropy of mixing, S^{mix}, can be written for fcc system using quasi-chemical solution model [18,19] as

$$S^{mix} = m_{pair}\gamma_{pair}S_{pair}^{mix} + m_{point}\gamma_{point}S_{point}^{mix} = 6S_{pair}^{mix} - 11S_{point}^{mix}$$

$$S_{pair}^{mix} = -R\,(yaa \ln yaa + 2yab \ln yab + ybb \ln ybb)$$

$$S_{point}^{mix} = -R\,(ya \ln ya + yb \ln yb)$$

$$yaa = \frac{1 - 2u_1 + u_2}{4},\ yab = \frac{1 - u_2}{4},\ ybb = \frac{1 + 2u_1 + u_2}{4}$$

$$ya = \frac{1 - u_1}{2},\ yb = \frac{1 + u_1}{2}$$

In this expression m represents the multiplicity and γ represents the correction to the entropy term, also known as Kikuchi-Barker coefficient [20], widely used in CVM frame work. In the above entropy expression, yij and yi represents the pair and point cluster variables respectively. These cluster variables are expressed using a set of independent variables, referred to as correlation function, in the orthogonal basis ($\tau_A = -1$ & $\tau_B = 1$). Thus, u_2 represents the pair correlation function and u_1 represents the point correlation. The point correlation function is related to the average composition of the system in the orthogonal basis [21] as

$$u_1 = 2x_B - 1$$

For the chosen energy parameter, T and composition, the energy of α phase should be minimum with respect to all the internal variables. Thus,

$$\frac{dG^{\alpha}}{du_2} = 0$$

This results in a quadratic equation in u_2 and can be solved for u_2 directly. The relevant solution obtained thus [22] is

$$u_2 = \frac{1 + \eta - 2\sqrt{\eta - u_1^2(\eta - 1)}}{\eta - 1}$$

where

$$\eta = \exp\left(-\frac{4w^{\alpha}}{RT}\right)$$

For the phase separating system, *i.e.*, $w^{\alpha} < 0$, the consolute point of the miscibility gap can be obtained by simultaneously solving the second and third derivatives of the Gibbs energy expression with respect to the composition to be zero. The consolute point is obtained as

$$x_{B,con} = 0.5 \text{ and } \eta_{con} = \frac{36}{25} = 1.44 \tag{2}$$

Thus,

$$T_{con}^{\alpha} = -\frac{4w^{\alpha}}{R \ln 1.44} \tag{3}$$

The expression for the miscibility gap is obtained as

$$T_{MG}^{\alpha} = -\frac{4w^{\alpha}}{R \ln\left[\frac{4u_1^2\left(1-u_1^2\right)^{\frac{1}{6}}}{\left(\left(1-u_1\right)^{\frac{1}{6}}\left(1+u_1\right)-\left(1-u_1\right)\left(1+u_1\right)^{\frac{1}{6}}\right)^2}\right]} \tag{4}$$

The high temperature phase, liquid, referred to as β, is modelled using the regular solution model. The reference energy can be expressed analogously to that of Eq. (1). The mixing energy is expressed using the regular solution approach as

$$G^{mix,\beta} = RT\left(x_A^{\beta} \ln x_A^{\beta} + x_B^{\beta} \ln x_B^{\beta}\right) + w^{\beta} x_A^{\beta} x_B^{\beta}$$

In the above expression $w^{\beta}$is the regular solution parameter. $w^{\alpha}$and $w^{\beta}$are referred to as energy parameters in the rest of this work.

The consolute point for the β phase is given by

$$x_{B,con} = 0.5 \text{ and } T_{con}^{\beta} = \frac{w^{\beta}}{2R} \tag{5}$$

while the locus of the miscibility gap boundary is obtained as [4]

$$T_{MG}^{\beta} = \frac{w^{\beta}\left(1-2x_B^{\beta}\right)}{R\ln\left[\frac{x_A^{\beta}}{x_B^{\beta}}\right]} \tag{6}$$

The chemical potential of the selected phase can be obtained using

$$\mu_A = G - x_B\frac{dG}{dx_B}$$
$$\mu_B = G + (1-x_B)\frac{dG}{dx_B}$$

At the thermodynamic equilibrium of α and β phases, the difference in the chemical potentials of the components for the phases vanishes simultaneously. Thus,

$$\begin{aligned}\mu_A^{\alpha} - \mu_A^{\beta} &= 0\\ \mu_B^{\alpha} - \mu_B^{\beta} &= 0\end{aligned} \tag{7}$$

The above equations contain difference in the standard Gibbs energy of the pure components $G_i^{0,\beta} - G_i^{0,\alpha}$. These terms are expressed as

$$G_i^{0,\beta} - G_i^{0,\alpha} = \Delta G_i = \Delta H_i - T\Delta S_i = \left(T_i - T\right)\Delta S_i$$

in which T_i represents the melting temperature of the component i and ΔS_i is the corresponding entropy of transformation.

2.2. Determination of the locus of an isomorphous system

The locus of the isomorphous system with and without a congruent extremum can be obtained with the help of the iso-G curve. The iso-G curve represents the locus of the composition and temperatures, (T_0, x_0), for which the Gibbs energy of the selected phases is equal [2]. For the chosen energy parameters, $w^{\alpha}$and w^{β}, the locus of iso-G points can be obtained using the following condition.

$$G^{\alpha}\left(w^{\alpha};T_0,x_0\right) = G^{\beta}\left(w^{\beta};T_0,x_0\right)$$

In the phase diagram, this iso-G curve passes through the two-phase region. For the system exhibiting congruent minimum (CMin) or maximum (CMax), iso-G curve also passes through this congruent point exhibiting minimum or maximum at the congruent point respectively.

For the system with $T_A < T_B$, the congruent minimum is observed for $0 < x_B < 0.5$ while the congruent maximum is observed for $0.5 < x_B < 1$. Thus, the slope of the iso-G curve for the congruent minimum system remains negative for $0 < x_B < x_{cong}$ and positive for $x_{cong} < x_B < 1$ where x_{cong} is the composition of the congruent minimum. The boundary for the limiting case, where the system transforms from simple isomorphous to the congruent minimum, can be obtained using

$$\lim_{x_0\to 0^+}\frac{dT_0}{dx_0} < 0$$

Similarly, the boundary of transformation from simple isomorphous to congruent maximum can be obtained using

$$\lim_{x_0\to 1^-}\frac{dT_0}{dx_0} > 0$$

For $T_A = 800$ K, $T_B = 1200$ K, with $\Delta S_A = \Delta S_B = 10$ J mol^{-1} K^{-1}, the boundary of the congruent minimum and maximum are calculated using the above conditions and are shown in Fig. 1. The boundaries of these reactions are indicated with '1' and '2', respectively, in the figure. The same thermodynamic parameters are used in the rest of this section for the calculation of boundaries for the other invariant reactions, unless otherwise specified.

2.3. Determination of the locus of peritectic (Peri) and monotectic (Mono) systems

As the miscibility gap boundary of the solid approaches the solidus boundary, the solidus boundary shows an inflection point [1] and can be observed in Fig. 2. The peritectic reaction occurs in the system exhibiting a miscibility gap in the solid phase and its interaction with the solidus boundary. Thus, the boundary of the peritectic reaction can be obtained by interaction of the maximum of the miscibility gap boundary with the solidus boundary. So, the composition of the solid phase on the solidus boundary is chosen to be 0.5, and the temperature of the invariant reaction is fixed at the consolute temperature given by Eq. (3). Since solid and liquid phases are in equilibrium, the conditions given in Eq. (7) are used to determine the unknown parameters. Thus, the mathematical conditions become

$$\begin{aligned}&x_{B,solidus} = x_{B,s} = 0.5 \text{ and } T = T_{con}^{\alpha}\\ &\mu_A^{\alpha}\left(w^{\alpha},T,x_{B,s}\right) = \mu_A^{\beta}\left(w^{\beta},T,x_B^{\beta}\right)\\ &\mu_B^{\alpha}\left(w^{\alpha},T,x_{B,s}\right) = \mu_B^{\beta}\left(w^{\beta},T,x_B^{\beta}\right)\end{aligned} \tag{8}$$

The above equations are solved to determine the locus of the peritectic reaction boundary for the chosen parameters. The boundary obtained using these conditions for the peritectic reaction is indicated with '3' in Fig. 1.

Analogous to the peritectic reaction, monotectic reaction occurs due to the interaction of miscibility gap in the liquid phase with the liquidus boundary. In the limiting case, the consolute point of the liquid phase just lies on the liquidus boundary and remains in equilibrium with the solid phase. Thus, the mathematical conditions for this case are similar to those mentioned in Eq. (8). The composition and temperature of the liquid phase can be fixed using the data given in Eq. (5), and the unknown parameters can be determined using the conditions given in Eq. (7). Using this data, the monotectic reaction boundary is determined and is shown in Fig. 1, labelled as '4'.

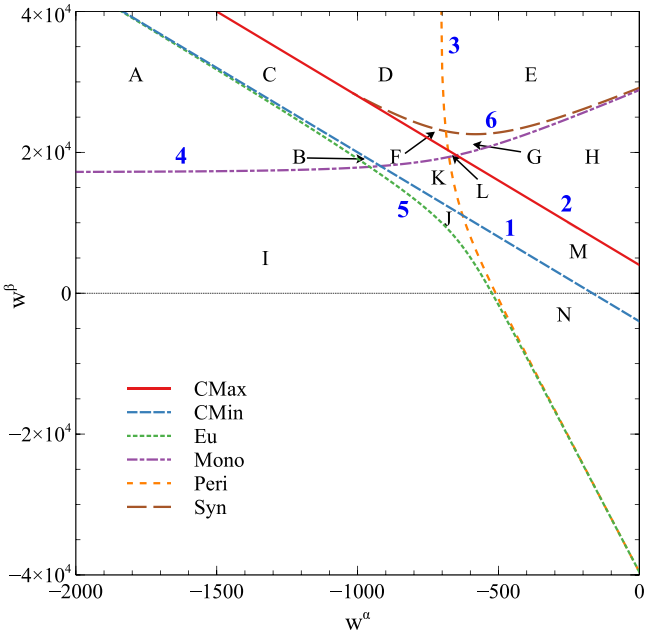


Fig. 1. The domains of various invariant reactions calculated for $\Delta S_A = \Delta S_B =$ 10 J mol^{-1} K^{-1}, $T_A = 800$ K and $T_B = 1200$ K.

2.4. Determination of the locus of eutectic (Eu) and syntectic (Syn) systems

A eutectic reaction occurs in the phase diagrams if the minimum of the iso-G curve lies within the miscibility gap of the low-temperature phase, *i.e.*, the solid phase. As the composition of the iso-G curve minimum moves towards the miscibility gap boundary, the difference in the composition of the liquid phase and one of the solid phases involved in the eutectic reaction decreases. If the minimum moves

outside the miscibility gap, the system exhibits a peritectic reaction with a congruent minimum. In this limiting case, the minimum in the iso-G curve lies on the miscibility gap. Thus, the composition of the minimum in the iso-G curve is equal to the composition of the miscibility gap boundary and the corresponding temperature is the invariant reaction temperature. Hence, $T_0 = T^{\alpha}_{MG}$ and $x_0 = x^{\alpha}_{B,MG}$. This data along with Eq. (7) are used to determine the boundary. The line indicated with '5' in Fig. 1 represents the boundary calculated thus for the eutectic reaction.

The interaction of the miscibility gap in the liquid phase with the maximum in the iso-G curve results in a syntectic reaction. The limiting boundary for the syntectic reaction can be determined following a similar procedure discussed for the eutectic reaction. In this case, the invariant reaction occurs at the congruent maximum temperature. At this temperature, $x_0 = x^{\beta}_{B,MG}$. Using this data along with the two phase equilibrium conditions is used to determine the locus of the syntectic reaction. The boundary calculated thus is labelled as '6' in Fig. 1.

3. Existence domains and the invariant reactions

Using the procedure mentioned in the previous section, the boundaries of invariant reaction for the phase separating interaction of the α phase are obtained and are shown in Fig. 1. The boundaries for peritectic and eutectic reactions occur primarily due to the interaction of the miscibility gap in the solid phase with the other phase boundaries. Consequently, these two reactions are limited by the vanishing of the miscibility gap in the solid phase for $w^{\alpha}= 0$. The lower limit for these reactions is therefore obtained by solving the conditions mentioned in the previous section for $w^{\alpha}= 0$ and is estimated to be approximately (0, −39519.8). As the value of w^{α}decreases, the eutectic boundary appears to approach the congruent minimum boundary asymptotically.

The monotectic boundary and the syntectic boundary also appear to meet each other asymptotically in the region where $w^{\alpha}> 0$ and $w^{\beta}> 0$ (not shown in Fig. 1). On the other limit, the syntectic boundary intersects the congruent maximum boundary at approximately (−1015.42, 28369.1).

The intersection of the invariant reaction boundaries results in various domains, within which different combinations of invariant reactions occur. The domains obtained using the parameters $\Delta S_A = \Delta S_B = 10$ J mol^{-1} K^{-1}, $T_A = 800$ K and $T_B = 1200$ K, along with the resulting invariant reactions, are listed below:

A – Eutectic (Eu) + Monotectic (Mono)
B – Congruent Minimum (CMin) + Peritectic (Peri) + Mono
C – Peri + Mono
D – Peri + Syntectic (Syn)
E – Miscibility gap (MG) + Syn
F – Peri + Mono + Congruent maximum (CMax)
G – MG + Mono + CMax
H – MG + CMax
I – Eu
J – CMin + Peri
K – Peri
L – MG + Mono
M – MG + Simple isomorphous (SI)
N – MG + CMin

The domain E extends to the other side where $w^{\alpha}> 0$. Since this region corresponds to ordering in the α phase, the resulting reaction in that domain is a syntectic reaction together with ordered phase regions at lower temperature. Similarly, the domains H, M, and N also extend to the other side, and the reactions expected in those domains are CMax with ordered phases, a simple isomorphous system with ordered phases, and CMin with ordered phases at lower temperatures, respectively. Based on the number of ordered phases stabilized under the approximation considered for a given system and their interaction with the high-temperature phase regions, various complex phase diagrams may be generated. This will be discussed elsewhere.

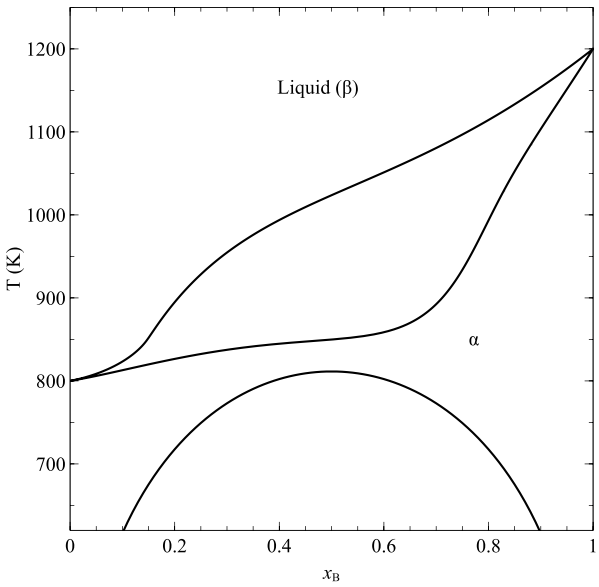


Fig. 2. Phase diagram calculated using w^{α} = −600 J mol^{-1}, w^{β}=11200 J mol^{-1} for the domain M. The phase diagram exhibits a misbilitygap in the solid phase.

Phase diagrams are calculated for specific values of (w^{α}, w^{β}) from domains M, A, B, D, and F and are shown in Figs. 2–6 respectively. As the values of these parameters vary within a domain, both the invariant reaction temperature and the equilibrium composition of the coexisting phases change. In domain I, where the eutectic reaction occurs, the invariant reaction data are obtained for different values of (w^{α}, w^{β}). The congruent minimum temperature in domain N and the monotectic temperature in domain A are also computed. Using this data, isothermal contours of the invariant reactions are plotted and is presented in Fig. 7. It is observed that the contours of the congruent minimum temperature are parallel to the congruent minimum boundary. The isothermal contours of the eutectic temperature are parallel to the w^{α}axis at lower values of $w^{\alpha}$and gradually align with the congruent minimum contours as they approach the eutectic boundary. It can also be observed that the change in eutectic temperature is small with increasing w^{β}, particularly at lower values of w^{α}. A similar behaviour is observed for the monotectic temperature. The contours of the peritectic reaction temperature in domain K and the congruent maximum temperature in the domain H are also calculated and shown in Fig. 8. It is observed that the contours of the congruent maximum temperature are parallel to the congruent maximum boundary, similar to those of the congruent minimum.

4. Application to the Cu-Ir system

4.1. Existence domains of the Cu-Ir system

In the previous section, the methodology for determining the domains of different invariant reactions is discussed for $\Delta S_A = \Delta S_B$ =10 J mol^{-1} K^{-1}, $T_A = 800$ K and $T_B = 1200$ K. Using the same methodology, the boundaries and domains of the invariant reactions can be obtained for any system. In the present work, this methodology is extended to the Cu-Ir system. Both Cu and Ir exist in fcc crystal structure at room temperature. This system exhibits a peritectic reaction together with a miscibility gap in the solid state. The peritectic reaction temperature is reported as 1138 ± 5 °C, with composition of the liquid phase at 4 at. % Ir and composition of the solid phases at 8 and 97 at. % Ir [23]. The thermodynamic data required for calculating the existence domains obtained from the SGTE database [24] is as follows:

ΔS_{Cu} = 9.7684 J mol^{-1} K^{-1}, ΔS_{Ir} =15.1247 J mol^{-1} K^{-1}, T_{Cu} = 1357.77 K and T_{Ir} = 2719 K.

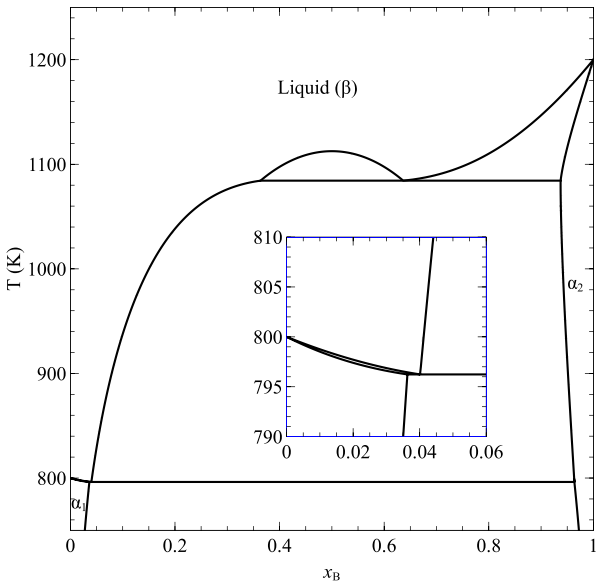


Fig. 3. Phase diagram calculated using w^{α} = −1000 J mol^{-1}, w^{β}=18500 J mol^{-1} for the domain A. The phase diagram exhibits a eutectic reaction at lower temperature and a monotectic reaction at higher temperature. The region of eutectic reaction is shown in the inset.

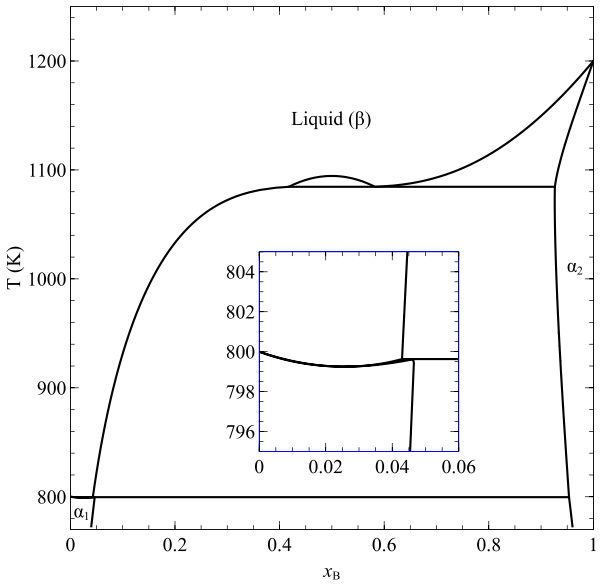


Fig. 4. Phase diagram calculated using w^{α} = −950 J mol^{-1}, w^{β}=18200 J mol^{-1} for the domain B. The phase diagram shows congruent minimum, peritectic reactions at lower temperature, and a monotectic reaction at higher temperature. The region of peritectic reaction with a congruent minimum is shown in the inset.

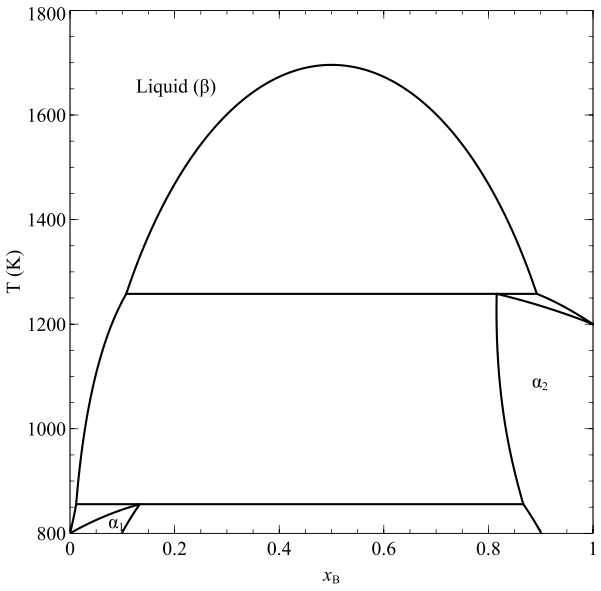


Fig. 5. Phase diagram calculated using w^{α} = −2000 J mol^{-1}, w^{β}=28200 J mol^{-1} corresponding to the domain D. The phase diagram shows a peritectic reaction at lower temperature and a syntectic (at higher temperature) reactions.

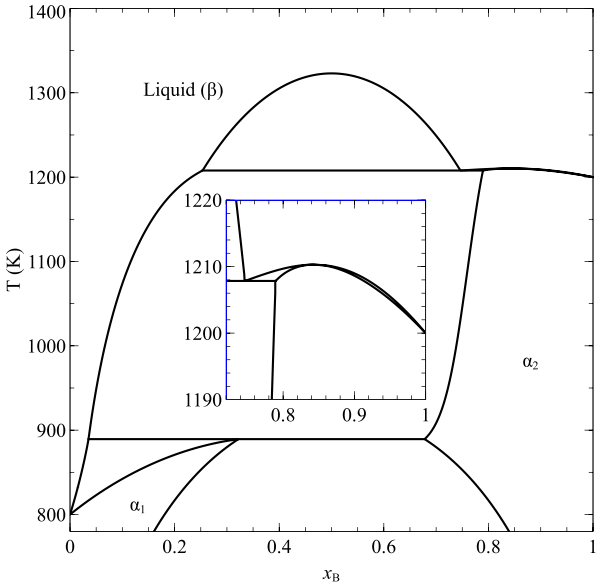


Fig. 6. Phase diagram calculated using w^{α} = −850 J mol^{-1}, w^{β}=24900 J mol^{-1} corresponding to the domain F. The phase diagram shows the peritectic reaction at lower temperature, monotectic, and congruent maximum reactions at higher temperature. The region of congruent maximum is shown in the inset.

The boundaries and domains of the invariant reactions are determined following the procedure discussed previously and are shown in Fig. 9. The labels of the invariant reaction boundaries and the domains remain the same as those mentioned in the previous section. It can be observed that the peritectic and monotectic reaction boundaries intersect above the congruent maximum boundary. This causes the disappearance of the monotectic reaction with a miscibility gap (domain L in Fig. 1) and gives rise to a new domain corresponding to peritectic reaction with a congruent maximum, labelled as O. Although there is not much change in the relative positions of the domains, a change in the scale of the axes should be noted. In the present case also the congruent maximum boundary and the syntectic reaction boundary intersect, and the point of the intersection is obtained as ≈ (−2578.13,75171.5).

The knowledge of these domains for the different invariant reactions is highly helpful in the selection of appropriate initial values of w^{α}, w^{β}during the optimization of the energy parameters. This process involves minimization of a merit function [25,26] defined as

$$\chi^2 = \sum_i \frac{e_i^2}{\sigma_i^2}$$

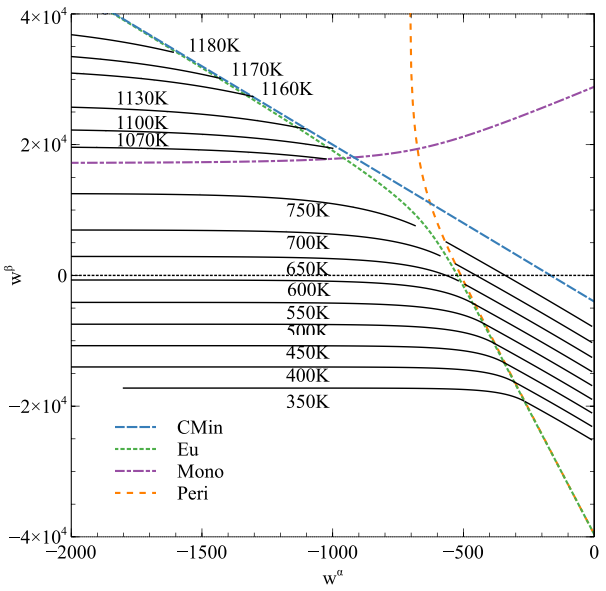


Fig. 7. The isothermal contours of the invariant reaction temperatures for eutectic, monotectic and congruent minimum reactions.

In this equation, e_i refers to the difference between the observed and the calculated values, and σ_i represents the standard deviation associated with the data point *i*. These data points can be compositions or temperatures of the phases in equilibrium on a phase boundary, or thermodynamic data such as enthalpy or latent heat. Thus, the merit function is highly complex and the energies of the phases involved in the optimization process are strongly coupled. The complexity further increases with an increase in the number of phases, and thereby the number of energy parameters. This merit function is minimized using iterative optimization methods such as Levenberg–Marquardt method [27] and these methods are highly sensitive to the initial values. Poor initial values may lead to an entirely incorrect phase diagram and cause the optimization process to fail. This process becomes highly cumbersome if the optimization process involves minimization of energy of the system with respect to internal variables. Thus, having an initial energy parameter set that results in a phase diagram at least qualitatively agrees with the experimental data significantly increases the likelihood of convergence.

Several approaches have been developed to predict appropriate initial values of the energy parameters. Gupta et al. proposed polynomials relating the consolute point, the curvature of the miscibility gap boundary at the consolute point, and the energy parameters. These polynomials can be solved for the available experimental phase diagram data or results from other computational methods such as DFT and Monte Carlo simulations to obtain reasonable estimates of the energy parameters. These can be used as initial values for the optimization process. A similar approach has also been extended to congruent point data for both fcc and bcc systems [28,29].

Existence domain diagrams are another effective method for selecting the initial values. Depending on the nature of the invariant reaction in the phase diagram, appropriate initial values can be chosen from the corresponding domains. These educated initial values generally lead to faster and efficient convergence of the merit function. Thakur et al. have used a similar approach to calculate the existence domains and optimized the energy parameters using temperature-composition phase boundaries of the Nb-Ti alloy system [8]. They demonstrated that the energy parameters obtained from the previous studies, as well as those resulting from their own optimization process, lie well within the relevant domain identified in their work. In the present work, artificial neural network is used to predict these energy parameters for the given invariant reaction data. The predicted energy parameters only minimize the error in the invariant reaction and the topology of the predicted phase diagram remains similar to the experimental diagram.

To contextualize the utility of the proposed supervised neural network framework, it is important to contrast it with modern CALPHAD parameter-optimization and uncertainty quantification workflows. Current state-of-the-art frameworks, such as the Extensible, Self-optimizing Phase Equilibria Infrastructure (ESPEI) [30], utilize Bayesian parameter estimation via Markov Chain Monte Carlo sampling to optimize thermodynamic parameters while propagating uncertainties. Though powerful, these probabilistic methods, alongside deterministic local optimizers such as the Levenberg–Marquardt algorithm [27], are heavily reliant on the quality of initial parameter inputs. Poor initial estimates frequently lead to convergence issues, high computational costs, or entrapment in unphysical local minima.

On the other hand, the supervised neural network method presented here addresses this bottleneck by acting as a high-fidelity initialization engine. Instead of conducting a blind or trial-and-error initialization, the network takes the invariant data as the input and predicts the optimal initial interaction parameters almost instantaneously. Additionally, while recent machine learning interatomic potential (MLIP)-to-CALPHAD workflows offer an ab-initio route to thermodynamic data generation, they require significant computational resources for training and atomistic simulations [31,32]. On the other hand, the approach presented in this work bypasses the atomistic scale and offers a rapid and direct mapping from macroscopic phase diagram topologies to thermodynamic interaction parameters.

4.2. Neural network modelling of the energy parameters

Machine learning methods have been extensively used for optimization tasks [33–36]. These algorithms can also be employed to generate suitable initial values required for the optimization process. Though a data point from the respective domain result in a topologically correct diagram, data from the existence domain used in conjunction with a trained supervised neural network model minimize the error between the experimental and calculated invariant reaction data. Since the Cu-Ir system exhibits a peritectic reaction, the data for neural network training and testing are selected from domain K of Fig. 9.

The neural network model is developed to predict the values of the energy parameters (w^{α}, w^{β}) as functions of temperature (T) and compositions x_B^{α} and x_B^{β}. In the following sections, we explain the data generation and preprocessing, the optimization of the neural network architecture, the performance metrics, and its application in providing the energy parameters for phase diagram optimization.

4.3. Database generation and preprocessing

The data for temperature and equilibrium compositions is generated using the quasi-chemical – regular solution model for various combinations of the energy parameters (w^{α},w^{β}). It is observed that the peritectic reaction occurs for $w^{\alpha} \in [-2585, -1082]$ J mol^{-1} and $w^{\beta} \in [5384, 44369]$ J mol^{-1}. The data points are generated using Python's *random* module with a seed of 1200 to ensure reproducibility. Using this, 1000 data points that belong to the domain K are generated. For each data point, the invariant reaction point is determined. Thus, a data base of 1000 random data points containing w^{α}, $w^{\beta}$and the corresponding peritectic reaction data is created. Further, data points from the database are chosen randomly and tested for the thermodynamic equilibrium once again. The database used in this work is given in the supplementary material.

In the database, the ranges of the parameters for the invariant reaction are T∈[1358, 1568] K and x_B^{α}, x_B^{β} ∈[0,1]. Since the magnitudes of the parameters in the database are significantly different from each other, it is important to normalize the data. This is a crucial step before

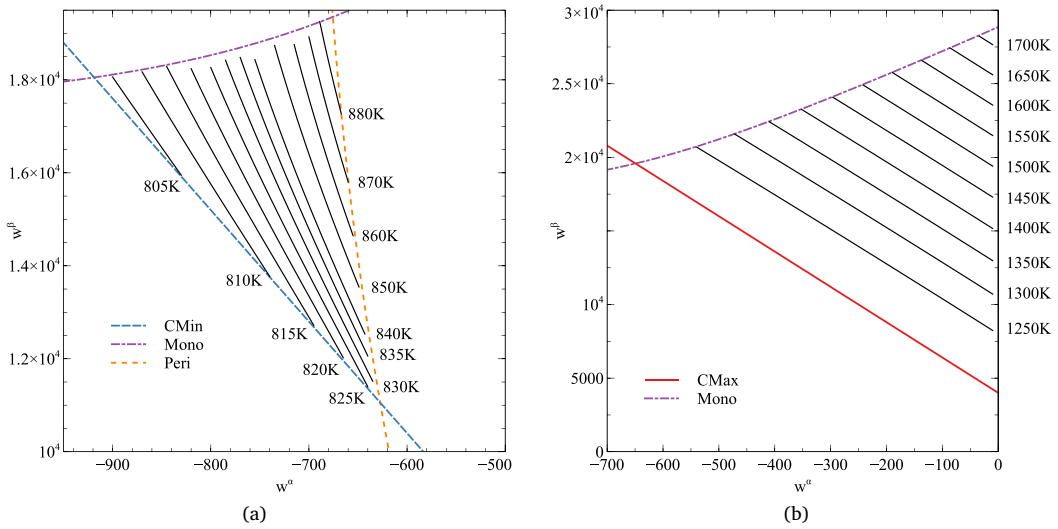


Fig. 8. Isothermal contours of invariant reaction temperatures for (a) peritectic and (b) congruent maximum reactions.

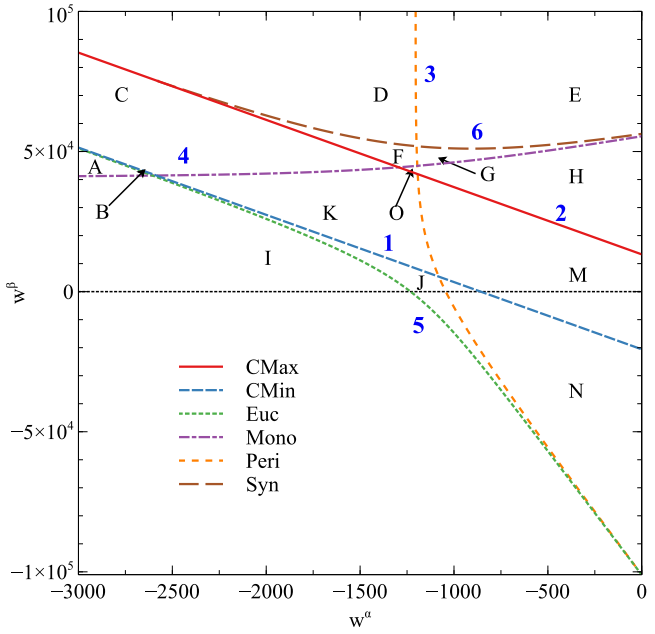


Fig. 9. The domains of invariant reactions for the Cu-Ir system with ΔS_{Cu} = 9.7684 J mol^{-1} K^{-1}, ΔS_{Ir} =15.1247 J mol^{-1} K^{-1}, T_{Cu} = 1357.77 K and T_{Ir} = 2719 K.

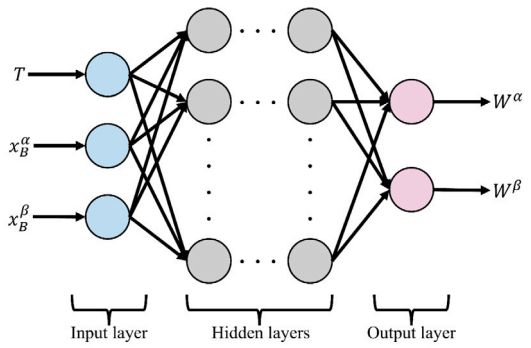


Fig. 10. A schematic representation of the neural network architecture used in this work.

using the data for training a neural network model. The data normalization step helps to eliminate the dominance of largely positive or negative data during neural network training, improve the convergence rate, and lead to better results [37–39]. All data in the database are normalized to the range [−1,1] using

$$x_n = 2\left(\frac{x - x_{min}}{x_{max} - x_{min}}\right) - 1 \tag{9}$$

where x_n is the normalized data, x is the input data, and x_{min} and x_{max} are the minimum and maximum values of the respective feature. The inverse of Eq. (9) is applied to rescale the predicted values back to their original scale after training or testing the neural network model.

4.4. Supervised neural network model

The temperatures and compositions are used as input features, while the energy parameters are predicted as outputs using a supervised neural network model [40–42]. A representative architecture of the supervised neural network model employed in this work is shown in Fig. 10. The input parameters are fed to the nodes of the input layer, and the predicted energy values are obtained from the nodes of the output layer. During training and testing of the model, a hyperbolic tangent (tanh) activation function is applied to the data at each hidden layer. Further, a linear activation function is applied to the data before passing it to the output layer. This is done in order to incorporate non-linearity in the model, which helps in capturing the complex correlations that exists between the input and output data [43,44]. Out of the 1000 data points generated, 80% are used exclusively for training the neural network model, and the remaining 20% are used for testing the model. The details of the libraries and parameters used for these calculations are provided in the appendix.

During training and testing of the neural network models, the accuracy of each model is quantified by comparing the predicted outputs with the corresponding actual values for the same set of input parameters. This assessment is performed using two metrics, viz., the root mean-squared error (RMSE) and the mean absolute error (MAE), mathematically expressed in Eqs. (10) and (11) respectively.

$$RMSE = \sqrt{\frac{1}{n}\sum_{i=1}^{n}\left(y_i^a - y_i^p\right)^2} \tag{10}$$

$$MAE = \frac{1}{n}\sum_{i=1}^{n}|y_i^a - y_i^p| \tag{11}$$

Table 1
Description of the neural network models and their performance.

Model number	Number of hidden layers	Number of nodes in hidden layer					RMSE		MAE	
		1	2	3	4	5	Training	Testing	Training	Testing
1	2	4	8	–	–	–	0.0207	0.0198	0.0293	0.0263
2	3	4	8	4	–	–	0.0207	0.0189	0.0278	0.0250
3	3	4	8	16	–	–	0.0148	0.0148	0.0208	0.0198
4	4	4	8	16	8	–	0.0194	0.0179	0.0258	0.0219
5	5	4	8	16	8	4	0.0146	0.0151	0.0203	0.0196
6	Linear least squares fit						0.1597	0.1572	0.1311	0.1297

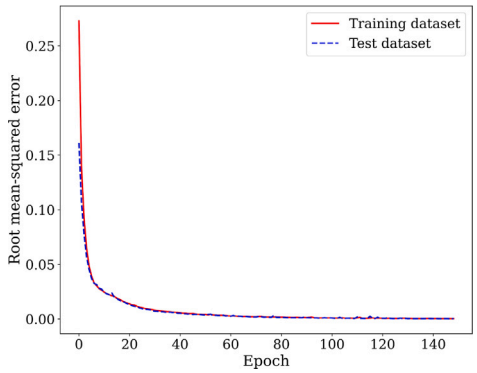


Fig. 11. The variation of RMSE loss with training cycle for the model 5.

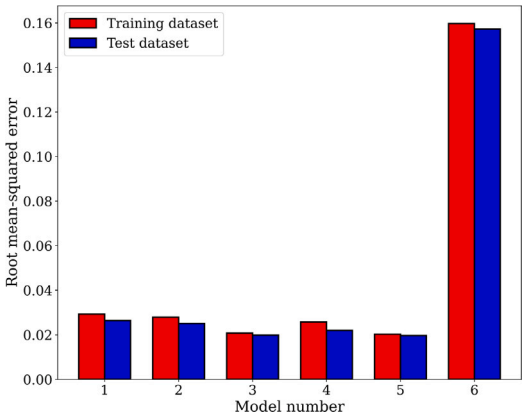


Fig. 12. Root mean-squared error loss for all the models used in this work.

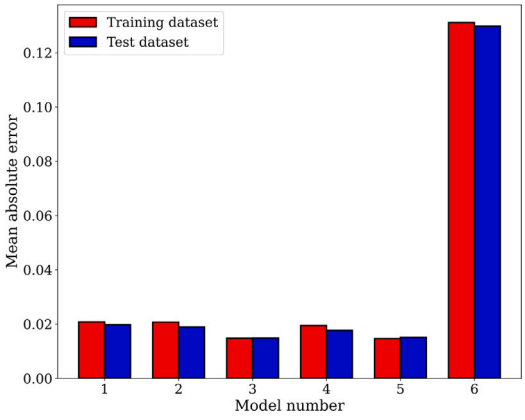


Fig. 13. Mean absolute error loss for all the models used in this work.

where n is the total number of data points, y_i^a and y_i^p are the actual and predicted values for the ith data point, respectively. RMSE penalizes larger deviations in the model-predicted output heavily due to its quadratic nature. On the other hand, MAE measures the average magnitude of errors and treat all errors linearly. The combination of these two metrics provides an interpretable average error and useful insight into the distribution of errors. Lower values of both RMSE and MAE indicate better predictive performance of the model.

A shallow neural network model may not be able to capture the complexities that exist between input and output data, whereas a deep neural network can be computationally expensive and requires substantial computational resources for training and testing. Therefore, to establish an optimal model, five different neural network architectures are trained. The detailed configurations of these neural networks is provided in Table 1. The loss curve for the model 5 is shown in Fig. 11.

The RMSE and MAE values calculated separately for the training and testing data sets for the neural networks as well as linear least squares fit after training and testing are presented in Table 1. The comparison of these values is shown in Figs. 12 and 13 respectively. Among these models, RMSE and MAE values are highest for the linear least squares fit. The energy values predicted are outside the domain. So, linear least squares fit is not considered further. While, for all the neural networks RMSE and MAE values are low and similar in magnitude for both training and testing data sets. This indicates that the trained models could predict the output reasonably well. The close agreement between the training and testing errors presented in Table 1 suggests that significant overfitting was not observed within the investigated parameter space. The networks are fed with the invariant data of the Cu-Ir peritectic reaction and the energy parameters are predicted. It is observed that the predicted energy parameters are with in the peritectic reaction domain. This reflects interpolation capability of the trained models with in the investigated domain. A boundary holdout strategy, in which selected temperature-composition regions are excluded during training and used exclusively for evaluation, could provide a more rigorous assessment of extrapolation performance and will be considered in future studies. The agreement between the experimental data and the calculated data can be improved further by using a deeper and wider neural network along with increase in the volume of the data. Since these energy values predicted using only the invariant reaction data are used as initial values for the thermodynamic inversion and optimization methodologies and require further refinement to agree with the other thermodynamic and phase diagram data, optimization of the neural network architecture is not considered further.

4.5. Phase diagram of the Cu-Ir system

D. J. Chakarabarthi and D. E. Laughlin evaluated the experimental and thermodynamic data of Cu-Ir system [23]. The invariant reaction data reported by them is used in the present work. The trained models are fed with this data, and the energy values are predicted. Since the RMSE and MAE values are low for the model 5 among the models

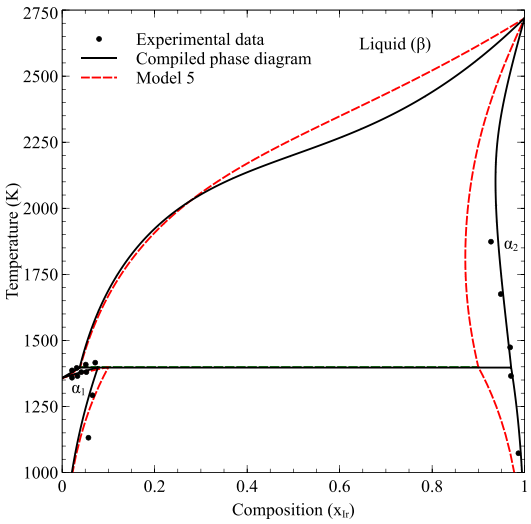


Fig. 14. Comparison of Cu-Ir phase diagram calculated using the energy parameters predicted by the model 5 and the phase diagram reproduced from [23].

considered, the corresponding energy values are used to calculate the phase diagram. The comparison of the phase diagrams computed using the predicted energy parameters along with the experimental data and the compiled phase diagram taken from [23] is shown in Fig. 14. The calculated phase diagram has topology similar to the experimental phase diagram. The deviation in the phase boundary on the Ir-rich end arise due to the limited number of energy parameters in the quasi-chemical and regular solution models. Thus, increasing the number of energy parameters in the thermodynamic models can improve the agreement in the solvus boundary on Ir rich end. Nevertheless, the neural network predicted energy parameters produced a phase diagram that resembles the experimental phase diagram.

It should be noted that the neural-network model developed in the present work is specific to the Cu-Ir binary system. Since temperature and composition are used as the only input features, the model does not explicitly incorporate elemental characteristics or thermodynamic descriptors that may govern the behaviour of other alloy systems. Consequently, the trained model should be regarded as a Cu-Ir specific surrogate model, and direct application to a different binary system would require retraining using an appropriate dataset. Furthermore, predictions outside the composition-temperature domain represented in the training dataset should be interpreted with caution because the model has not been validated under extrapolative conditions. The current framework only provides a benchmark for utilization of existence domains in conjunction with the artificial neural network to predict the initial estimates of the energy parameters for the optimization process using the phase diagram data.

5. Conclusions and future work

Using the quasi-chemical solution approach the solid phase is modelled, while the high temperature liquid phase is modelled using the regular solution model. The invariant reactions in the phase diagram are treated as the interaction of the miscibility gap of one of the phases with the solidus, liquidus, or iso-G boundaries. Using the appropriate thermodynamic conditions for the chosen solution models, the loci of energies corresponding to congruent minimum, congruent maximum, eutectic, peritectic, monotectic, and syntectic reactions are determined for a prototype binary system. The isothermal contours of these invariant reactions, illustrating the behaviour of the system within their respective domains are also presented.

The developed methodology is applied to the Cu-Ir binary system, which exhibits a peritectic reaction with a miscibility gap in the solid phase at low temperatures. The existence domain boundaries are calculated for this system, and the invariant reaction data corresponding to the peritectic domain are generated. These data are used to train a supervised artificial neural network model to predict the energy parameters of both solid and liquid phases. In the model, temperature (T) and compositions (x_{Ir}^{α}, x_{Ir}^{β}) served as inputs, while energy parameters (w^{α}, w^{β}) are predicted as outputs. The phase diagram calculated using the neural network predicted energy parameters shows a good agreement with the reported experimental phase diagram for the Cu-Ir system, with some deviations in solubility on the Ir-rich side. These deviations are attributed to the limited number of energy parameters in the selected solution models. Thus, the proposed methodology can be used to get a reliable set of initial values for the inversion methods used to determine the energy parameters using experimental or theoretical phase diagram data as well as thermodynamic data. The proposed neural-network model should be viewed as an inverse surrogate framework for generating physically reasonable initial estimates of interaction energy parameters rather than as a replacement for established thermodynamic inversion and optimization methodologies. Extension of the methodology to other alloy systems would require retraining with appropriate data such as elemental and thermodynamic descriptors to improve model transferability and enable the development of more generalized predictive frameworks.

It should be noted that the linear least-squares model employed for comparison serves as a simple reference baseline illustrating the benefits of nonlinear learning. Future work may consider comparisons with more advanced inversion and regression methodologies to further assess the relative strengths and limitations of neural-network-based approaches. It also includes extending the developed methodology for existence domain calculations for more complex solution models that provide short range order parameters and are computationally intensive. Furthermore, the supervised neural network model for predicting the energy parameters can be integrated with multiscale computational frameworks, including density functional theory (DFT), CALPHAD, and phase-field modelling for microstructure evolution and property prediction [45–47]. Advanced architectures such as graph neural networks and long short-term memory (LSTM) networks can also be explored to enhance predictive accuracy and enable inverse design of alloy compositions [48,49]. These extensions are expected to broaden the applicability of the approach presented in this work to complex materials systems and accelerate data-driven alloy development.

CRediT authorship contribution statement

Rajendra Prasad Gorrey: Conceptualization, thermodynamic modelling, doamins calculations, methodology, supervision, investigation, formal analysis, validation, writing – original draft, review & editing, . **Monish Kumar Dharanilogan:** Domain calculations, neural network modelling and calculations, development of codes, visualization, validation, investigation, data curation. **Abhishek Kumar Thakur:** Writing – review & editing, Writing – original draft, visualization, supervision, methodology, conceptualization.

Declaration of competing interest

The authors declare that they have no known competing financial interests or personal relationships that could have appeared to influence the work reported in this paper.

Appendix A. Supplementary data

Libraries and parameters used for machine learning

The machine learning calculations are carried out on Kaggle. The libraries used for machine learning are:

Library	Version
Python	3.12.12
Keras	3.10.0
Numpy	2.0.2
Pandas	2.3.3
Scikit-Learn	1.6.1
Tensorflow	2.19.0

Adam optimizer is used with batch size=16 and validation split = 0.2. Default values are used for all the remaining parameters. In these calculations, validation loss is monitored with minimum value of delta as 10E-4. To avoid over fitting, early stopping method is employed. If there is not significant improvement in validation loss for 15 consecutive epochs, the training is terminated and the weights corresponding to the best known model are restored.

Supplementary material related to this article can be found online at https://doi.org/10.1016/j.calphad.2026.102999.

Data availability

The data will be made available upon reasonable request.

References

[1] J.J.V. Laar, Die Schmelz-oder Erstarrungskurven bei binären Systemen, wenn die feste Phase ein Gemisch (amorphe feste Lösung oder Mischkristalle) der beiden Komponenten ist, Z. Phys. Chem. 63 (1908) 216—-253.

[2] J.J.V. Laar, Melting or solidification curves in binary system, Z. Phys. Chem. 63 (1908) 216.

[3] A.D. Pelton, W.T. Thompson, Phase diagrams, Prog. Solid State Chem. 10 (PART 3) (1975) 119–155, http://dx.doi.org/10.1016/0079-6786(75)90004-7.

[4] H.A.J. Oonk, Phase Theory: The Thermodynamics of Heterogeneous Equilibria, Elsevier, Amsterdam, 1981.

[5] R.T. DeHoff, Thermodynamics in materials science, McGraw-Hill, New York, 1993.

[6] Y.A. Chang, S.L. Chen, Thermodynamics of metallic solutions, in: N. Sano, M. Maeda, K.W. Lu, P. Riboud (Eds.), Advanced Physical Chemistry for Process Metallurgy, Academic Press, Sandiago, USA, 1997, p. 5.

[7] B.N. Sarma, S.S. Prasad, S. Vijayvergiya, V.B. Kumar, S. Lele, Existence domains for invariant reactions in binary regular solution phase diagrams exhibiting two phases, Bull. Mater. Sci. 26 (4) (2003) 423–430, http://dx.doi.org/10.1007/BF02711187.

[8] A.K. Thakur, V.K. Pandey, V. Jindal, Calculation of existence domains and optimized phase diagram for the Nb-Ti binary alloy system using computational methods, J. Phase Equilibria Diffus. 41 (6) (2020) 846–858, http://dx.doi.org/10.1007/s11669-020-00843-z.

[9] R. Kikuchi, A theory of cooperative phenomena, Phys. Rev. 81 (6) (1951) 988–1003, http://dx.doi.org/10.1103/PhysRev.81.988.

[10] W.A. Oates, H. Wenzl, The cluster/site approximation for multicomponent solutions - a practical alternative to the cluster variation method, Scr. Mater. 35 (5) (1996) 623–627, http://dx.doi.org/10.1016/1359-6462(96)00198-4.

[11] Y.Y. Li, Quasi-chemical method in the statistical theory of regular mixtures, Phys. Rev. 76 (7) (1949) 972–979, http://dx.doi.org/10.1103/PhysRev.76.972.

[12] C.N. Yang, A generalization of the quasi - chemical method in the statistical theory of superlattices, J. Chem. Phys. 13 (2) (1945) 66–76, http://dx.doi.org/10.1063/1.1724001.

[13] C.L. Fu, R.P. Gorrey, B.C. Zhou, A cluster-based computational thermodynamics framework with intrinsic chemical short-range order: Part I. Configurational contribution, Acta Mater. 277 (2024) http://dx.doi.org/10.1016/j.actamat.2024.120138.

[14] J.M. Sanchez, T. Mohri, Approximate solutions to the cluster variation free energies by the variable basis cluster expansion, Comput. Mater. Sci. 122 (2016) 301–306, http://dx.doi.org/10.1016/j.commatsci.2016.05.035.

[15] R.P. Gorrey, V. Jindal, B.N. Sarma, S. Lele, Polynomial functions for configurational correlation functions in gibbs energies of solid solutions using cluster variation method, Comput. Mater. Sci. 186 (2021) 109746, http://dx.doi.org/10.1016/j.commatsci.2020.109746.

[16] H.L. Lukas, E.T. Henig, B. Zimmermann, Optimization of phase diagrams by a least squares method using simultaneously different types of data, Calphad 1 (3) (1977) 225–236, http://dx.doi.org/10.1016/0364-5916(77)90002-5.

[17] C.W. Bale, A.D. Pelton, Optimization of binary thermodynamic and phase diagram data, Met. Trans. B 14 (1) (1983) 77–83, http://dx.doi.org/10.1007/BF02670872.

[18] E.A. Guggenheim, Mixtures: The Theory of the Equlibrium Properties of Some Simple Classes of Mixtures Solutions and Alloys, Clarendon Press, 1952.

[19] H.L. Lukas, S.G. Fries, B. Sundman, Computational Thermodynamics : The CALPHAD Method, Cambridge University Press, 2007, p. 313.

[20] J.A. Barker, Methods of approximation in the theory of regular mixtures, Proc. R. Soc. Lond. A 216 (1124) (1953) 45–56, http://dx.doi.org/10.1098/rspa.1953.0005.

[21] G. Inden, Atomic ordering, in: G. Kostorz (Ed.), Phase Transformations in Materials, Wiley-Blackwell, 2005, pp. 519–581, http://dx.doi.org/10.1002/352760264X.ch8.

[22] R.P. Gorrey, V. Jindal, B.N. Sarma, S. Lele, Thermodynamics of binary bcc and fcc phases for exclusive second-neighbour pair interactions using cluster variation method: Analytical solutions, Trans. Indian Inst. Met. 75 (5) (2022) 1365–1381, http://dx.doi.org/10.1007/s12666-021-02469-2.

[23] D.J. Chakrabarti, D.E. Laughlin, The Cu-Ir (copper-iridium) system, J. Phase Equilib. 8 (2) (1987) 132–136, http://dx.doi.org/10.1007/BF02873198.

[24] A.T. Dinsdale, SGTE data for pure elements, Calphad 15 (4) (1991) 317–425, http://dx.doi.org/10.1016/0364-5916(91)90030-N.

[25] S. Lele, B.N. Sarma, Computational thermodynamics of Sc-Zr and Sc-Ti alloys using cluster variation method, in: Journal of Materials Science, 44, (9) 2009, pp. 2334–2342, http://dx.doi.org/10.1007/s10853-008-3197-6.

[26] B. Nageswara Sarma, Computation of Optimized Binary Phase Diagrams Exhibiting CPH and BCC Phases uisng Cluster Variation Method (Ph.D. thesis), Institute of Technology, Banaras Hindu University, 2000.

[27] W.H. Press, S.A. Teukolsky, W.T. Vetterling, B.P. Flannery, Numerical Recipes : The Art of Scientific Computing, third ed., Cambridge University Press, 2007, p. 1235.

[28] G.S. Gupta, G.V. Madhav, A. Pandey, B.N. Sarma, S. Lele, Estimation of CE-CVM energy parameters from miscibility gap data, Bull. Mater. Sci. 28 (2) (2005) 173–177, http://dx.doi.org/10.1007/BF02704237.

[29] G.S. Gupta, Estimation of Energy Parameters for Optimization using Cluster Variation Method (Ph.D. thesis), Institute of Technology, Banaras Hindu University, 2008.

[30] B. Bocklund, R. Otis, A. Egorov, A. Obaied, I. Roslyakova, Z.K. Liu, ESPEI for efficient thermodynamic database development, modification, and uncertainty quantification: Application to Cu-Mg, MRS Commun. 9 (2) (2019) 618–627, http://dx.doi.org/10.1557/mrc.2019.59.

[31] C.W. Rosenbrock, K. Gubaev, A.V. Shapeev, L.B. Pártay, N. Bernstein, G. Csányi, G.L. Hart, Machine-learned interatomic potentials for alloys and alloy phase diagrams, Npj Comput. Mater. 7 (1) (2021) http://dx.doi.org/10.1038/s41524-020-00477-2, arXiv:1906.07816.

[32] S. Zhu, D. Sarıtürk, R. Arróyave, Accelerating CALPHAD-based phase diagram predictions in complex alloys using universal machine learning potentials: Opportunities and challenges, Acta Mater. 286 (2025) http://dx.doi.org/10.1016/j.actamat.2025.120747, arXiv:2411.15351.

[33] A.K. Thakur, R.P. Gorrey, V. Jindal, K. Muralidharan, A data-driven approach to approximate the correlation functions in cluster variation method, Modelling Simul. Mater. Sci. Eng. 30 (1) (2022) 015001, http://dx.doi.org/10.1088/1361-651X/ac3a16.

[34] I. Papadimitriou, I. Gialampoukidis, S. Vrochidis, I. Kompatsiaris, AI methods in materials design, discovery and manufacturing: A review, Comput. Mater. Sci. 235 (2024) http://dx.doi.org/10.1016/j.commatsci.2024.112793.

[35] F. Conrad, J.P. Stöcker, C. Signorini, I. de Paula Salgado, H. Wiemer, M. Kaliske, S. Ihlenfeldt, Exploring design space: Machine learning for multi-objective materials design optimization with enhanced evaluation strategies, Comput. Mater. Sci. 246 (2025) http://dx.doi.org/10.1016/j.commatsci.2024.113432.

[36] L. Lian, W. Li, Y. Zhang, X. Gong, W. Hu, Y. Liu, Design of Ni-based single crystal superalloys by machine learning based on data-driven multi-task optimization, Comput. Mater. Sci. 256 (2025) http://dx.doi.org/10.1016/j.commatsci.2025.113969.

[37] J. Sola, J. Sevilla, Importance of input data normalization for the application of neural networks to complex industrial problems, IEEE Trans. Nucl. Sci. 44 (3 PART 3) (1997) 1464–1468, http://dx.doi.org/10.1109/23.589532.

[38] S. Srinivasan, M.Z. Saghir, Modeling of thermotransport phenomenon in metal alloys using artificial neural networks, Appl. Math. Model. 37 (5) (2013) 2850–2869, http://dx.doi.org/10.1016/j.apm.2012.06.018.

[39] S. Fidan, H. Oktay, S. Polat, S. Ozturk, An artificial neural network model to predict the thermal properties of concrete using different neurons and activation functions, Adv. Mater. Sci. Eng. 2019 (2019) 1–13, http://dx.doi.org/10.1155/2019/3831813.

[40] J. Schmidt, M.R.G. Marques, S. Botti, M.A.L. Marques, Recent advances and applications of machine learning in solid-state materials science, Npj Comput. Mater. 5 (1) (2019) 83, http://dx.doi.org/10.1038/s41524-019-0221-0.

[41] A. Paszke, S. Gross, F. Massa, A. Lerer, J. Bradbury, G. Chanan, T. Killeen, Z. Lin, N. Gimelshein, L. Antiga, A. Desmaison, A. Köpf, E. Yang, Z. DeVito, M. Raison, A. Tejani, S. Chilamkurthy, B. Steiner, L. Fang, J. Bai, S. Chintala, Pytorch: An imperative style, high-performance deep learning library, Adv. Neural Inf. Process. Syst. 32 (2019) arXiv:1912.01703.

[42] A.K. Thakur, S.N. Totade, K. Muralidharan, M. Dutta, Phase diagram determination using machine learning methods in materials science and engineering: a review, Phil. Mag. 106 (2) (2026) 180–204, http://dx.doi.org/10.1080/14786435.2025.2558154.

[43] X. Glorot, Y. Bengio, Understanding the difficulty of training deep feedforward neural networks, in: Proceedings of the Thirteenth International Conference on Artificial Intelligence and Statistics, 2010, pp. 249–256, URL https://proceedings.mlr.press/v9/glorot10a.html.

[44] S.R. Dubey, S.K. Singh, B.B. Chaudhuri, Activation functions in deep learning: A comprehensive survey and benchmark, Neurocomputing 503 (2022) 92–108, http://dx.doi.org/10.1016/j.neucom.2022.06.111.

[45] A. Kumar Thakur, S. Kovacevic, V.R. Manga, P.A. Deymier, K. Muralidharan, A first-principles and CALPHAD-assisted phase-field model for microstructure evolution: Application to mo-v binary alloy systems, Mater. Des. 235 (2023) 112443, http://dx.doi.org/10.1016/j.matdes.2023.112443.

[46] T. Morino, M. Ode, S. Hirosawa, An explicit integration approach for predicting the microstructures of multicomponent alloys, Nat. Commun. 16 (1) (2025) http://dx.doi.org/10.1038/s41467-025-61246-7.

[47] C. Shen, The synergy of machine learning and CALPHAD: Revitalizing traditional approaches, Comput. Mater. Sci. 258 (2025) http://dx.doi.org/10.1016/j.commatsci.2025.113970.

[48] Y. Qin, S. DeWitt, B. Radhakrishnan, G. Biros, GrainNN: A neighbor-aware long short-term memory network for predicting microstructure evolution during polycrystalline grain formation, Comput. Mater. Sci. 218 (2023) http://dx.doi.org/10.1016/j.commatsci.2022.111927.

[49] H. Razavi, N. Moelans, Physics-informed GCN-LSTM framework for long-term forecasting of 2D and 3D microstructure evolution, Npj Comput. Mater (2026) http://dx.doi.org/10.1038/s41524-026-01999-x.